Research Square

Preprints are preliminary reports that have not undergone peer review.
They should not be considered conclusive, used to inform clinical practice,
or referenced by the media as validated information.

Nontrivial spin and orbital textures in YbMn2Ge2

Junzhang Ma

junzhama@cityu.edu.hk

City University of Hong Kong https://orcid.org/0000-0002-4648-3576

Xin Liang

City University of Hong Kong

Weihang Liang

Zhejiang University

Yutong Feng

East China Normal University

Zihan Lin

Department of Physics, The City University of Hong Kong, Kowloon

Yuhao Wang

East China Normal University

Fazhi Yang

City University of Hong Kong

Tianhao Guo

City University of Hong Kong

Siyu Heng

City University of Hong Kong

Wenlong Lu

Department of Physics, The City University of Hong Kong, Kowloon

Shiyu Feng

City University of Hong Kong

Ming Shi

Zhejiang University https://orcid.org/0000-0002-6090-8219

Yu Mao

Zhejiang University https://orcid.org/0009-0004-3958-0169

Tian Shang

East China Normal University https://orcid.org/0000-0002-5916-0020

Yuanfeng Xu

Zhejiang University https://orcid.org/0000-0002-1390-2308

Article

Keywords:

Posted Date: August 22nd, 2026

DOI: https://doi.org/10.21203/rs.3.rs-10721601/v1

License: This work is licensed under a Creative Commons Attribution 4.0 International License.
Read Full License

Additional Declarations: There is **NO** Competing Interest.

Nontrivial spin and orbital textures in $YbMn_2Ge_2$

Xin Liang[1,†], Weihang Liang[2,†], Yutong Feng[3,†], Zihan Lin[1,†], Yuhao Wang[3], Fazhi Yang[1], Yu Mao[2], Tianhao Guo[1], Siyu Heng[1], Wenlong Lu[1], Shiyu Feng[1], Ming Shi[2,4], Tian Shang[3,5*], Yuanfeng Xu[2,*], Junzhang Ma[1,*]

[1]*Department of Physics, City University of Hong Kong; Kowloon, Hong Kong, China.*

[2] *Center for Correlated Matter and School of Physics, Zhejiang University; Hangzhou 310058, China.*

[3] *School of Physics, East China Normal University; Shanghai 200241, China.*

[4]*Institute for Advanced Study in Physics, Zhejiang University; Hangzhou 310058, China.*

[5]*Key Laboratory of Polar Materials and Devices (MOE), East China Normal University; Shanghai 200241, China.*

† These authors contributed equally to this work

* Corresponding to: tshang@phy.ecnu.edu.cn, y.xu@zju.edu.cn, junzhama@cityu.edu.hk

Altermagnetism has attracted considerable research interest as a new platform for spintronic functionalities without net magnetization. Extending altermagnetism to two dimensions is highly desirable for applications but remains challenging because the symmetries of most two-dimensional (2D) collinear magnetic materials preserve spin degeneracy, rendering experimentally verified intrinsic two-dimensional altermagnets elusive in bulk materials. Recent theoretical advances demonstrate a route to two-dimensional altermagnetism through surface-induced symmetry breaking in layered antiferromagnetic materials. Using angle-resolved photoemission spectroscopy and first-principles calculations, we directly resolve such intrinsic 2D altermagnetic electronic states on the surface of $YbMn_2Ge_2$ that emerge despite the magnetically compensated bulk order. These surface states are guaranteed by the quantized Berry phase of the bulk states which enforces their emergence at the terminating surface. Beyond the realization of pure 2D altermagnetism, we further identify a symmetry-protected p-wave orbital angular momentum texture localized at the surface, revealing an orbital analogue of unconventional p-wave magnetic order. Moreover, the anomalous Hall effect (AHE) is observed, which is unexpected in pristine $YbMn_2Ge_2$ with combined time reversal and inversion symmetry (PT). Our work experimentally establishes antiferromagnetic surfaces as a realizable versatile platform for realizing two-dimensional altermagnetism and uncovers a route toward spin–orbital quantum phenomena in magnetic materials.

Altermagnetism has recently emerged as a new paradigm of magnetism, attracting considerable attention in condensed matter physics and spintronics research[1–3]. Although altermagnets possess compensated collinear magnetic configurations, they exhibit non-relativistic momentum-dependent spin splitting and magnetotransport and electronic responses typically associated with ferromagnets[4–22]. At the same time, altermagnets retain key advantages of antiferromagnets, including ultrafast terahertz dynamics, robustness against external magnetic fields, and absence of stray fields[7,23,24]. These unconventional properties originate from the interplay between specific crystal and magnetic symmetries, which enable exchange-driven spin splitting without relying on relativistic spin-orbit coupling[2,3,25]. As a result, altermagnets provide a fundamentally new platform for spin manipulation and information processing[26,27]. While experimental and theoretical efforts have rapidly expanded the family of three-dimensional (3D) altermagnets, extending altermagnetism into the 2D limit remains a major challenge[28,29]. The experimental study of 2D altermagnets is limited to a few systems, including the hidden ordered altermagnetic phase RV_2Se_2O family with a G-type antiferromagnetic (AFM) structure[30–36] and intercalated transition metal dichalcogenides[37–39], as experimentally realized intrinsic 2D altermagnetism remains elusive to date. The realization of intrinsic 2D altermagnetism is particularly important because reduced dimensionality not only enables efficient electrostatic, strain, and interfacial control, but also provides a natural platform for integrating altermagnetic functionalities into device architectures[40–42]. More fundamentally, confinement to two dimensions can enhance the effect of physical phenomena and stabilize unconventional spin, orbital, charge order, and topological states that are hard to access in bulk materials. However, realizing intrinsic 2D altermagnetism is fundamentally challenging because the magnetic and crystal symmetries required to produce momentum-dependent spin splitting are difficult to satisfy in most of the reported 2D collinear magnets[28,29,33]. In particular, many experimentally accessible 2D antiferromagnets retain the combined PT symmetry that preserves spin degeneracy, preventing the emergence of altermagnetic band splitting[43]. Consequently, experimentally accessible 2D altermagnetic materials remain exceedingly rare, motivating the search for alternative design strategies. Rather than searching for intrinsically 2D altermagnets, an alternative strategy is to engineer altermagnetism through symmetry reduction at the surface of conventional antiferromagnets.

Recent theoretical studies have suggested that crystal termination provides a natural route to 2D altermagnetism through surface-induced symmetry breaking[44–46]. In many collinear antiferromagnets, spin degeneracy is protected in the bulk by inversion- or translation-related spin sublattices. Crystal termination removes the inversion and translational symmetries that relate opposite-spin sublattices in the bulk, while preserving the local rotational symmetry of magnetic sites. Consequently, the symmetry protecting bulk spin degeneracy is lifted, allowing momentum-dependent spin splitting to emerge at the surface[45,46]. As a result, the surface may acquire the defining symmetry characteristics of an altermagnet, giving rise to momentum-dependent spin splitting despite the magnetically compensated bulk state. Furthermore, the reduced surface symmetry also allows a finite non-trivial Berry curvature, and associated transport responses, including the AHE and the generation of spin-polarized currents [47–49], offering a promising platform for spintronic applications. This concept transforms the search for 2D altermagnets from identifying rare intrinsic materials to engineering altermagnetic states through surface symmetry breaking in conventional antiferromagnets, which will greatly expand the pool of candidate materials beyond intrinsically altermagnetic compounds.

Here, we demonstrate this concept experimentally in the layered AFM metal $YbMn_2Ge_2$ (YMG) (Figs. 1a-c), an ideal candidate for realizing surface altermagnetism[44]. While bulk YMG remains PT symmetric and spin-degenerate, surface-induced symmetry breaking is predicted to generate *d*-wave spin polarized states characteristic of altermagnetism. Using high-resolution angle-resolved photoemission spectroscopy (ARPES), circular-dichroism (CD) ARPES and first-principles calculations, we directly observe the symmetry-protected surface states in YMG that exhibit the characteristic *d*-wave altermagnetic electronic structure (Figs. 1d, e). We further reveal a momentum-dependent *p*-wave orbital texture associated with these states (Figs. 1f, g). These findings provide direct evidence for emergent 2D altermagnetism at the surface of a conventional antiferromagnet and demonstrate a general strategy for engineering altermagnetic and orbital phenomena through surface-symmetry breaking. In addition, magnetotransport measurements reveal the presence of an AHE, suggesting the activation of Berry-curvature-related transport in the high magnetic field. Together, these results establish YMG as a model platform for investigating the interplay between altermagnetism, orbital angular momentum textures, and band topology in low-dimensional systems[50–53].

Basic information of YMG

YMG is a layered metallic antiferromagnet adopting a $ThCr_2Si_2$-type body-centered tetragonal structure (Fig. 1a) with a space group of I4/mmm[44,54]. The room-temperature lattice parameters are a=4.05Å and c=10.84Å. The Yb atoms occupy the Wyckoff position 2a site (0,0,0), the Mn atoms occupy the Wyckoff position 4d site (0,1/2,1/4), and the Ge atoms occupy the Wyckoff position 4e site (0,0, z). It undergoes an AFM transition at $T_N \sim 510$ K, according to previous studies[54–58]. The unit cell has a quadruple-layered structure stacked along the c-axis, with a center of inversion at Yb (Fig. 1a). The compound undergoes two magnetic phase transitions from the paramagnetic phase to AFM-I (Fig. 1b) and to AFM-II (Fig. 1c) across a temperature range spanning from ambient conditions to low temperature, accompanied by a temperature-dependent valence state in Ytterbium (Yb)[54–58]. In the AFM-I phase, the Mn magnetic moments form a collinear AFM order, which undergoes a secondary transition to an AFM-II phase at 165 K. Previous studies suggest that the Yb ions in this compound exist in a mixed-valence state between divalent (Yb^{2+}) and trivalent (Yb^{3+})[54,56]. The instability of these Yb valence states is thought to significantly influence the magnetic structure of the Mn sublattice. X-ray photoemission spectroscopy (Fig. 1i) reveals the elemental composition of the sample, and the X-ray diffraction (XRD) pattern (Fig. 1j) shows sharp (00l) reflections, demonstrating the high crystalline quality of the crystals. Band-structure calculations (Fig. 1k) reveal a high density of states (DOS) at the Fermi level, primarily dominated by Yb 4f electrons. Multi-orbital Hubbard model calculations further indicate that the metallic AFM state in YMG arises from a delicate balance between electronic correlations and partial Fermi surface nesting, which stabilizes AFM order without the formation of a full charge gap[44].

Band structure and surface states of YMG

To establish the electronic band structure of YMG, we first mapped its 3D band dispersion with varying photon energies. As shown in Fig. 2a, ultraviolet (UV) photon-energy-dependent scans between 60 and 130 eV were conducted to precisely determine the k_z dependence of the electronic states and locate the high-symmetry points Γ and Z in the Fermi surface map along the k_x-k_z. Despite the layered structure of YMG, several bands near the center of the projected BZ exhibit dispersion, indicating a finite degree of 3D electronic character. By analyzing the experimental photon-energy-dependent mapping (Fig. 2) and considering the crystal lattice constant c = 10.86

Å, we identify photon energies of 117 eV and 103 eV as corresponding to the Γ and Z points, respectively. Representative Fermi surface maps measured at different photon energies are shown in Figs. 2d-i. Three sets of pockets were observed, denoted as α, β, and γ. Notably, apart from the evolution of the α pockets at the center versus photon energy, the square β pocket and the two intersecting elliptical γ pockets remain essentially unchanged over all photon energies, as shown in Figs. 2d-i. By comparison with the calculations in Figs. 2b, c, we further confirm that the β and γ pockets correspond to surface states.

Figure 3 presents detailed results of the Fermi-surface topology and the low-energy electronic structure of YMG at the $k_z = 0$ (Γ) and π (Z) planes. Figure 3a shows a three-dimensional electronic structure at the Γ plane, illustrating the in-plane band dispersion and the locations of high-symmetry points. Fermi surface maps measured at the Z plane (Fig. 3b) exhibit flower-petal pockets (α) surrounding the zone center contributed from more than one band, together with a square-like Fermi surface (β) and two intersecting elliptical γ pockets, whereas the center of the Γ plane (Fig. 3c) is dominated by a compact rhomboid profile at the center (α), but β and γ pockets remain essentially the same as those in the Z plane. These distinct Fermi-surface geometries reflect the strong momentum dependence of the low-energy electronic structure. Band dispersions along high-symmetry directions are shown in Figs. 3d-g (the three sets of band dispersion are tracked with light-blue, black and red dashed lines). Along the Z-Γ direction (cut 1), linearly dispersing β bands intersect near the Fermi level, forming a Dirac-like electronic structure, while α bands have a small hole-like dispersion in the vicinity of the Z point and the γ band exhibits electron-like dispersion near the BZ corner, as shown in Fig. 3f. Both the α bands and β bands are observed along the Y-Z direction, confirming that the α and β pockets at the Z plane originate from hole carriers. In contrast, band structures along the X-Γ (cut 3) and the S-G directions (cut 4), reveal electron-like pockets (α bands) centered at the Γ point, coexisting with the previously identified β and γ bands. The nearly unchanged dispersions of the β and γ bands across different kz values further support their surface origin. The ARPES raw spectra are plotted in Fig. S1 of the Supplementary Materials.

The surface states can be understood in terms of the Berry phase of the occupied bulk states at the charge-neutrality point. The bulk spectrum remains fully gapped at charge neutrality along the one-

dimensional path (π, π, k_z), which projects onto the $\bar{M}$ point of the surface Brillouin zone. The corresponding Berry phase is

$$\gamma = \oint_{BZ} \mathrm{Tr}[\mathbf{A}(k_z)]\, \mathrm{d}k_z \pmod{2\pi} = \pi$$

where the integration is performed along the path from (π, π, -π) to (π, π, π) in the BZ of the conventional unit cell, and $\mathbf{A}(k_z)$ denotes the non-Abelian Berry connection matrix of the occupied bands. This quantized Berry phase indicates the emergence of an in-gap state at the surface $\bar{M}$ point when the cleavage plane passes through the $z = 0$ plane (Fig.1a), analogous to the boundary state of the SSH chain or the surface states of an obstructed atomic insulator[59–63]. The calculated electronic structures in Fig. S2 demonstrate the emergence of these surface states. Compared with the corresponding bulk calculations, additional surface-derived bands are clearly observed in the surface-projected band structures, with their associated features also appearing in the Fermi-surface maps. These surface states are present in both the calculations with and without SOC.

Observation of AHE

To establish the magnetic properties of YMG, we performed systematic magnetization and magnetotransport measurements (Fig. 4). Both the temperature-dependent magnetization M(T) (Fig. 4a) and longitudinal electrical resistivity ρ_{xx}(T) (Fig. 4b) exhibit a distinct magnetic transition at T_{N1} = 165 K, consistent with the onset of the low-temperature AFM phase reported previously[54–58]. Upon applying an external magnetic field, an additional field-induced magnetic transition emerges at T_{N2} below T_{N1}. While T_{N1} remains insensitive to the magnetic field, T_{N2} increases with the magnetic field, and eventually approaches T_{N1} at high magnetic field. The field-induced phase transition is further evidenced by the magnetization M(H). For $T < T_{N2}$, M(H) (Fig. 4c) exhibits a step-like anomaly at $\mu_0 H_c \approx$ 5–6 T, indicating the presence of spin reorientation. In contrast, for $T > T_{N2}$, such a metamagnetic transition is absent in the M(H) curve. Simultaneously, the field-dependent resistivity ρ_{xx}(H) exhibits a distinct anomaly at the same critical field for $T \leq T_{N2}$ (Fig. 4d). The close correspondence between the magnetic and transport anomalies demonstrates a strong coupling between the magnetic structure and the electronic states in YMG.

The most striking feature appears in the Hall response. As shown in Fig. 4e, the typical Hall resistivity ρ_{yx}(H) collected at 100 K exhibits a step-like increase at $\mu_0 H \sim 5$ T, coinciding with the

M(H) data in Fig. 4c. Similar behaviors were observed for all the $\rho_{yx}(H)$ curves for temperatures below T_{N2} (see Supplementary Materials Fig. S3). In contrast, for $T > T_{N2}$, $\rho_{yx}(H)$ evolves smoothly with magnetic field and displays the conventional nonlinear behavior expected from multiband charge transport. To quantify the Hall response, $\rho_{yx}(H)$ data were decomposed into ordinary and anomalous contributions according to $\rho_{yx}(H) = \rho_{yx}^{OHE} + \rho_{yx}^{AHE}$, where ρ_{yx}^{OHE} and ρ_{yx}^{AHE} represent the ordinary Hall effect (OHE) and AHE, respectively. The OHE is described by the conventional two-band model, and the AHE is fitted with $\rho_{yx}^{AHE} = R_s M$[64–66].

The extracted anomalous Hall resistivity, ρ_{yx}^{AHE}, becomes finite only for $H > Hc$ at $T \leq T_{N2}$. This is clearly summarized in the $\rho_{yx}^{AHE}(H,T)$ contour plot in Fig. 4f. Combining the field- and temperature-dependent magnetization and transport measurements allows the magnetic phase diagram of YMG to be established, revealing three distinct AFM phases, i.e., AFM-I, AFM-II, and AFM-III. Remarkably, the AHE is only observed in the AFM-III phase, while it is absent in both the AFM-I and AFM-II phases, indicating the close relationship between AHE and the underlying magnetic symmetry. It also indicates that the field-induced magnetic reconstruction activates a finite Berry-curvature response in the high-field antiferromagnetic state.

In the low-field AFM-II or AFM-I phase, the combined PT symmetry imposes a cancellation of Berry curvature and thus suppresses an intrinsic AHE. Although the surface states identified by ARPES break inversion symmetry and exhibit momentum-dependent spin and orbital textures, the remaining surface symmetries may still enforce compensation of the integrated Berry curvature, resulting in a vanishing net anomalous Hall conductivity. In the high-field AFM-III phase, however, these symmetry constraints are relaxed, allowing a finite Berry curvature and enabling the AHE. The present data do not allow us to unambiguously separate bulk and surface contributions to the anomalous Hall conductivity. Nevertheless, the onset of AHE only in the high-field phase demonstrates that the field-induced magnetic reconstruction activates finite Berry curvature, with the surface altermagnetic states providing an additional symmetry-allowed channel for anomalous Hall transport.

Symmetry Analysis and SOC effect

Termination of the crystal breaks inversion symmetry along the surface normal direction, reducing the bulk symmetry and enabling the emergence of surface-localized electronic states[67]. To understand the properties of the orbital and spin states, we analyze their symmetry properties

within a group-theoretical framework. Below the Néel temperature T_N = 510 K, YMG exhibits layered AFM order, with the Mn moments antiparallel between the adjacent layers and tilted with an angle θ relative to the [001] direction. Upon warming, θ increases from about 62° at 35K to 90° at 165K[54–56]. For θ < 90° (AFM II), the system belongs to the magnetic space group (MSG) *Pnnm'*(BCS setting 58.396), with generators $\{C_{2y}, M_x\tau, PT\}$, where τ denotes the translation vector (1/2, 1/2, 1/2). When θ = 90° (AFM I), the MSG becomes *Im'mm* (BCS setting 71.535), with generators $\{C_{2y}, M_x, PT\}$.

To elucidate the role of magnetic symmetry, we performed density functional theory (DFT) calculations for these two magnetic configurations, with and without spin–orbit coupling (SOC) as shown in Fig. S4. The overall band dispersions are nearly identical across the different calculations, indicating that SOC and the spin canting act primarily as perturbations to the electronic structure, although symmetry breaking produces subtle differences at certain high-symmetry points. This implies that SOC is weak in YMG and that the essential symmetries can be understood within the nonrelativistic spin-group framework[2,3], where spin and real-space transformations are treated independently.

Orbital angular momentum pattern

A spin group element is written as $[R_s||R|\,\tau]$, where R_s denotes an operation in spin space, R represents a point-group operation acting only in real space, and τ denotes a translation. For the AFM-I Phase (θ = 90°), the spin space group has generators {[-1||C_{2z}|0]T, [-1||C_{4z}|0], [1||m_x|0]}. For the AFM-II phase (θ < 90°), the space group has generators {[C_{2y}||C_{2z}|0]T, [C_{2z}||C_{4z}|0], [1||m_x|0]}. Therefore, the symmetry and momentum-space distribution of those emergent spin and orbital textures slightly depend on the orientation of the magnetic moments (θ).

Although the spin-space parts of the spin groups differ between the two phases, their real-space operations are identical. Since the orbital angular momentum is insensitive to the spin-space part of the spin-group operations in the nonrelativistic limit, the orbital textures in both phases follow the same symmetry constraints. The surface symmetry operations impose strong constraints on the orbital angular momentum of the electronic states, forcing the out-of-plane component to vanish identically, $L_z(k_x, k_y) = 0$. The orbital texture is therefore confined to the (k_x, k_y) plane. The in-plane components obey four independent symmetry relations (Table 1): L_x is even under $k_y \rightarrow -k_y$, whereas L_y is odd. Under C_{4z}, L_x and L_y transform into one another with relative signs

determined by the rotation direction. Accordingly, L_x is odd under $k_x \rightarrow -k_x$ and odd under inversion of (k_x, k_y). These constraints produce symmetry-protected nodal structures and sign reversals across the nodal directions, yielding *p*-wave-like textures for both L_x and L_y, as shown in Figs. 5a, b.

Table 1: Symmetry constraints on the orbital and spin textures of the surface states in the AFM-I and AFM-II phases in the absence of SOC.

Type	SSG Symmetry on the (001) surface	Orbital texture	Spin texture
AFM I (colinear)	$[-1\|\|C_{2z}\|0]$ T $[-1\|\|C_{4z}\|0]$ $[1\|\|m_x\|0]$	$L_z = 0$ $L_y(k_x, k_y) = -L_x(-k_y, k_x)$ $L_x(k_x, k_y) = L_y(-k_y, k_x)$ $L_x(k_x, k_y) = L_x(-k_x, k_y)$ $L_y(k_x, k_y) = -L_y(-k_x, k_y)$	$S(k_x, k_y) = -S(-k_y, k_x)$ $S(k_x, k_y) = S(-k_x, k_y)$
AFM II (non-colinear)	$[C_{2y}\|\|C_{2z}\|0]$ T $[C_{2z}\|\|C_{4z}\|0]$ $[1\|\|m_x\|0]$	*Same as above*	$S_y = 0$ $S_x(k_x, k_y) = -S_x(-k_y, k_x)$ $S_z(k_x, k_y) = -S_z(-k_y, k_x)$ $S_x(k_x, k_y) = S_x(-k_x, k_y)$ $S_z(k_x, k_y) = S_z(-k_x, k_y)$

More specifically, L_x and L_y exhibit orthogonal *p*-wave symmetries and together form a two-component in-plane *p*-wave orbital texture. The total in-plane orbital angular momentum (L_x, L_y) varies continuously in momentum space and satisfies $L(k_x, k_y) = - L(-k_x, -k_y)$ due to the presence of the antiunitary spin-group symmetry $[R_s||E|0]T$, whose real-space part is the identity while the time-reversal operation reverses both the momentum and the orbital angular momentum. Unlike the individual components, the combined vector field has no symmetry-enforced nodal directions except at the zone center, where the orbital polarization vanishes. This texture resembles the nodal-less p_x+ip_y structure proposed for unconventional superconductors[68]. Because spin and orbital degrees of freedom are decoupled without SOC, the calculated orbital textures remain nearly identical in the AFM-I and AFM-II phases.

CD-ARPES proof of orbital angular momentum

To experimentally probe the orbital character of these surface states, we performed circular-dichroism ARPES (CD-ARPES) measurements. The dichroic Fermi surface map (Fig. 5c) shows a distinct antisymmetric intensity pattern, providing direct evidence for momentum-dependent orbital polarization. The spectra reveal a clear sign reversal across the M_{xy} mirror plane. The

alternating dichroic patterns (red-blue) reflect a nontrivial p-wave-like orbital angular momentum texture and agree well with the symmetry-allowed orbital polarization expected for the surface states (Fig. 5d). The quantity measured in our CD-ARPES experiment corresponds to a projection of the orbital angular momentum onto the experimental detection geometry rather than the full vector field. When projected along the (110) direction, the underlying orbital texture gives rise to a pronounced nodal *p*-wave pattern, as shown in Fig. 5d. This nodal structure originates from the C_{4z} rotational symmetry of the surface electronic orbits, which relates the L_x and L_y components under successive 90-degree rotations. As a consequence, the projected texture ($L_x\mathrm{Sin}(\pi/4) + L_y\mathrm{Cos}(\pi/4)$) possesses a sign reversal under M_{xy} mirror operation. The observed dichroic signal therefore represents a projected manifestation of an underlying two-component *p*-wave orbital texture governed by the reduced surface symmetry, which agrees well with the calculations.

_d_-wave spin pattern

We now turn to the spin texture of the surface states. In both the AFM-I and AFM-II phases, the surface S_x component obeys the same spin-group symmetry constraints:

$$S_x(k_x, k_y) = -S_x(-k_y, k_x),\ S_x(k_x, k_y) = S_x(-k_x, k_y)$$

These relations require symmetry-imposed sign reversals of $S_x$between neighboring momentum quadrants. Consequently, unlike the bulk bands, the surface states exhibit a pronounced momentum-dependent spin texture. Under the rotation C_{4z}, the spin polarization alternates between adjacent quadrants, producing a two-dimensional *d*-wave altermagnetic pattern for both $\theta = 90°$ and $\theta < 90°$ (Figs. 5e,f and Fig. S5). The calculated surface band structure along high-symmetry directions [Fig. 5e] further reveals spin reversals along the Γ-X and Γ-Y directions, consistent with the expected altermagnetic symmetry. For the AFM-I phase, the collinear magnetic structure permits an arbitrary spin-quantization axis in the absence of SOC; the spin texture is therefore characterized by the symmetry of the spin polarization rather than a fixed crystallographic direction. In the canted AFM-II phase, the reduced magnetic symmetry allows additional relative spin components. Because the Mn moments lie in the *xz* plane, surface symmetry enforces $S_y = 0$, while S_x and S_z follow the d-wave symmetry relations summarized in Table 1. For example, the calculated S_x texture (Fig. 5f) shows the characteristic of *d*-wave pattern, demonstrating the

robustness of the surface altermagnetic spin texture against magnetic canting, consistent with previous theoretical predictions[44].

The cases when considering SOC

When SOC is included, the symmetry-protected relationships are summarized in Supplementary Materials Table S1. Nevertheless, the calculated spin textures and orbital angular momentum textures shown in Fig. S5 exhibit only minor deviations from those without SOC. The overall momentum-dependent sign alternation and nodal structure remain largely intact, indicating that the *d*-wave altermagnetic spin texture and *p*-wave orbital texture are remarkably robust. The coexistence of *d*-wave spin and *p*-wave-like orbital textures highlights the novel spin and orbital degrees of freedom that emerge from surface-induced symmetry breaking.

Conclusion and outlook

In summary, we experimentally establish YMG as a platform for emergent two-dimensional altermagnetism arising from surface-induced symmetry breaking. By combining momentum-resolved photoemission spectroscopy, first-principles calculations, and symmetry analysis, we identify surface-localized electronic states that host the characteristic *d*-wave altermagnetic spin texture while remaining embedded within a magnetically compensated antiferromagnetic bulk. Beyond the spin degree of freedom, we further uncover a two-component momentum-dependent *p*-wave orbital texture arising from the same reduced surface symmetry, revealing an orbital counterpart to the unconventional *p*-wave magnetic order. These results demonstrate that crystal termination alone can transform the surface of a conventional antiferromagnet into an effective two-dimensional altermagnetic state, providing a general route for realizing altermagnetic states without requiring intrinsically altermagnetic materials. More broadly, our work establishes antiferromagnetic surfaces as a fertile platform for symmetry engineering in quantum materials. The coexistence of unconventional spin and orbital textures offers new opportunities to manipulate Berry curvature, spin-orbit coupling, and topological electronic states through surface symmetry, electrostatic gating, strain, or structure design. We anticipate that this surface-engineering approach will stimulate the discovery of new altermagnetic materials and provide a foundation for developing scalable antiferromagnetic spin-orbitronic devices based on symmetry-protected quantum functionalities.

Methods

Crystal growth and characterization of YMG crystals

High-quality YMG single crystals were grown using a molten-In-flux method. High-purity Yb pieces (Prmat 99.9%), Mn granules (Thermo Fisher Scientific 99.99%), Ge granules (Aladdin, 99.999%), and In ingots (Prmat, 99.9999%) in a ratio of 1:2:2:40 were loaded in an alumina crucible and sealed in a quartz ampule. The quartz ampule was then heated to 1100 °C at a rate of 200 °C/h. After annealing at this temperature for more than 24 h, the ampule was slowly cooled to 700°C at a rate of 2 °C/h. After removing the excess In flux using a centrifuge, single crystals with typical dimensions 2 mm × 2 mm × 0.8 mm were obtained, which have a rectangular shape.

Crystal structure (phase purity) and orientation were checked by x-ray diffraction at room temperature using a Panalytical Empyrean x-ray diffractometer with Cu Kα radiation. The atomic ratios of the YMG single crystals were checked by energy dispersive x-ray spectra (EDS) installed on a field-emitting scanning electron microscope (FE-SEM, Hitachi S-4800). The measured Yb: Mn: Ge ratio was 21.2: 40.4: 38.4, which is almost identical to the stoichiometric ratio. The electrical transport and magnetic properties were measured in a Quantum Design physical property measurement system and magnetic properties measurement system, and in a cryogen-free magnetic property measurement system. For the above measurements, the magnetic field was applied along the c-axis ($H \parallel c$) of the YMG single crystal. For the transport measurements, the electric current was applied within the ab-plane ($I \parallel ab$). To avoid spurious transport contributions due to misaligned Hall contacts, the longitudinal contribution to the Hall resistivity ρ_{yx}, was removed by an antisymmetrization procedure, i.e., $\rho_{yx}(H) = \left[\rho_{yx}(H) - \rho_{yx}(-H)\right]/2$. Whereas, in the case of the longitudinal electrical resistivity ρ_{xx}, the spurious transverse contribution was removed by a symmetrization procedure, i.e., $\rho_{xx}(H) = [\rho_{xx}(H) + \rho_{xx}(-H)]/2$.

ARPES measurements of the sample

Conventional angle-resolved photoemission spectroscopy (ARPES) measurements were performed at beamline BL03U of the Shanghai Synchrotron Radiation Facility (SSRF), utilizing energy and angular resolutions of approximately 20 meV and 0.1°, respectively, at a sample temperature of 32 K. Circular dichroism ARPES (CD-ARPES) experiments were carried out at SSRF “dream line” 09U with an energy resolution of 100 meV at 11 K. Soft X-ray ARPES (SX-

ARPES) measurements were conducted at beamline BL25SU of the SPring-8 synchrotron radiation source, with energy and angular resolutions set to 60 meV and 0.1°, respectively, at a temperature of 77 K (liquid nitrogen cooling). Spin-resolved ARPES (SARPES) measurements were performed at beamline BL5U of the UVSOR synchrotron facility, featuring an energy resolution of 10 meV at a temperature of 20 K and at the Bloch beamline of MAX IV, where the branchline 2 endstation is dedicated to spin-resolved ARPES measurements and is equipped with a high-efficiency VLEED detector and a SPECS spin-rotator package, enabling resolution of all three spin polarization components. Room-temperature ARPES measurements were also performed at branchline 1 of the Bloch beamline at MAX IV. All crystal samples were cleaved in situ and maintained throughout the measurements under ultra-high vacuum (UHV) conditions better than 2×10^{-10} Torr.

DFT calculations

The DFT calculations were performed using the Vienna Ab initio Simulation Package (VASP)[69]. We performed calculations with different choices of the Coulomb repulsion U, and we found that U = 3 eV shows the best agreement with the experimental results (the converged magnetic moments and corresponding canting angles obtained for different Hubbard U values as shown in Table. SII). Therefore, we set U=3 eV in all calculations, unless noted otherwise. For the canted magnetic configuration, the calculation was initialized with a magnetic moment of $\mu = 3.2\mu B$ per Mn atom and a canting angle of $\theta = 30°$. The converged magnetic moment magnitudes and canting angles are summarized in Table1. At U = 3eV, the final magnetic moment is $\mu = 3.95\mu B$ with a canting angle of 88.3°. An energy cutoff of 600 eV and a 13 × 13 × 7 Γ-centered k-mesh were employed. The band structure obtained from the PBE method was fitted to a tight-binding model Hamiltonian using the maximally projected Wannier function method, which was then used to calculate the Fermi surface with the WannierTools package[72–73].

Data and materials availability: All data needed to evaluate the conclusions in the paper are present in the paper and/or the Supplementary Materials. Materials and additional data related to this paper may be requested from the authors.

Acknowledgements

We acknowledge Prof. Lin Jiao for useful discussions and primary investigation of the surface topology and properties of the single crystals. We acknowledge Prof. Lunhui Hu for useful discussion. This work was supported by the National Key R&D Program of China (grant no. 2025YFA1411500), the National Natural Science Foundation of China (12422405, 12550401 and 12374163, 12374105, 12350710785, 12561160109), by the Hong Kong Research Grants Council via Early Career Scheme (21304023), by the Hong Kong Collaborative Research Fund (Grant No. C604624G, and C1018-22E), by the The NSFC/RGC Collaborative Research Scheme CRS_CityU101/25 and CRS_HKUST603/25, by the Zhejiang Provincial Natural Science Foundation of China (Grant No. LR26A040003); F.Y. gratefully acknowledges the support by the fellowship awards from the Research Grants Council of Hong Kong (Project No. CityU JRFS2627-1S12); We acknowledge the MAX IV Laboratory for beamtime on the BLOCH beamline under proposal 20221394. Research conducted at MAX IV, a Swedish national user facility, is supported by Vetenskapsrådet (Swedish Research Council, VR) under contract 2018-07152, Vinnova (Swedish Governmental Agency for Innovation Systems) under contract 2018-04969 and Formas under contract 2019-02496. We thank the Shanghai Synchrotron Radiation Facility (SSRF) of BL03U (https://cstr.cn/31124.02.SSRF.BL03U), BL09U (https://cstr.cn/31124.02.SSRF.BL09U) for the assistance on ARPES measurements. We acknowledge the SPring-8 for time on the Beamline BL25SU (Proposals No. 2025A1613, No. 2025B1698). We acknowledge UVSOR Synchrotron Facility, Institute for Molecular Science for time on Beamline BL5U, BL7U with assistance from the beamline scientists (IMS program 25IMS6658, 25IMS6869).

Author contributions

J.Z.M. supervised this project. X.L. and Z.H.L performed ARPES experiments with the help of F.Z.Y., T.H.G., S.Y.H., W.L.L. and S.Y.F.; X.L., W.H.L., and Y.T.F. plotted the figures; W.H.L. and Y.F.X. performed the theoretical analysis and the first-principles calculations of the band structure. Y.T.F., W.Y.H. and T. S. synthesized the single crystals and characterized their transport properties. X.L. and J.Z.M. wrote the manuscript with input from all authors.

Competing interests: The authors declare that they have no competing interests.

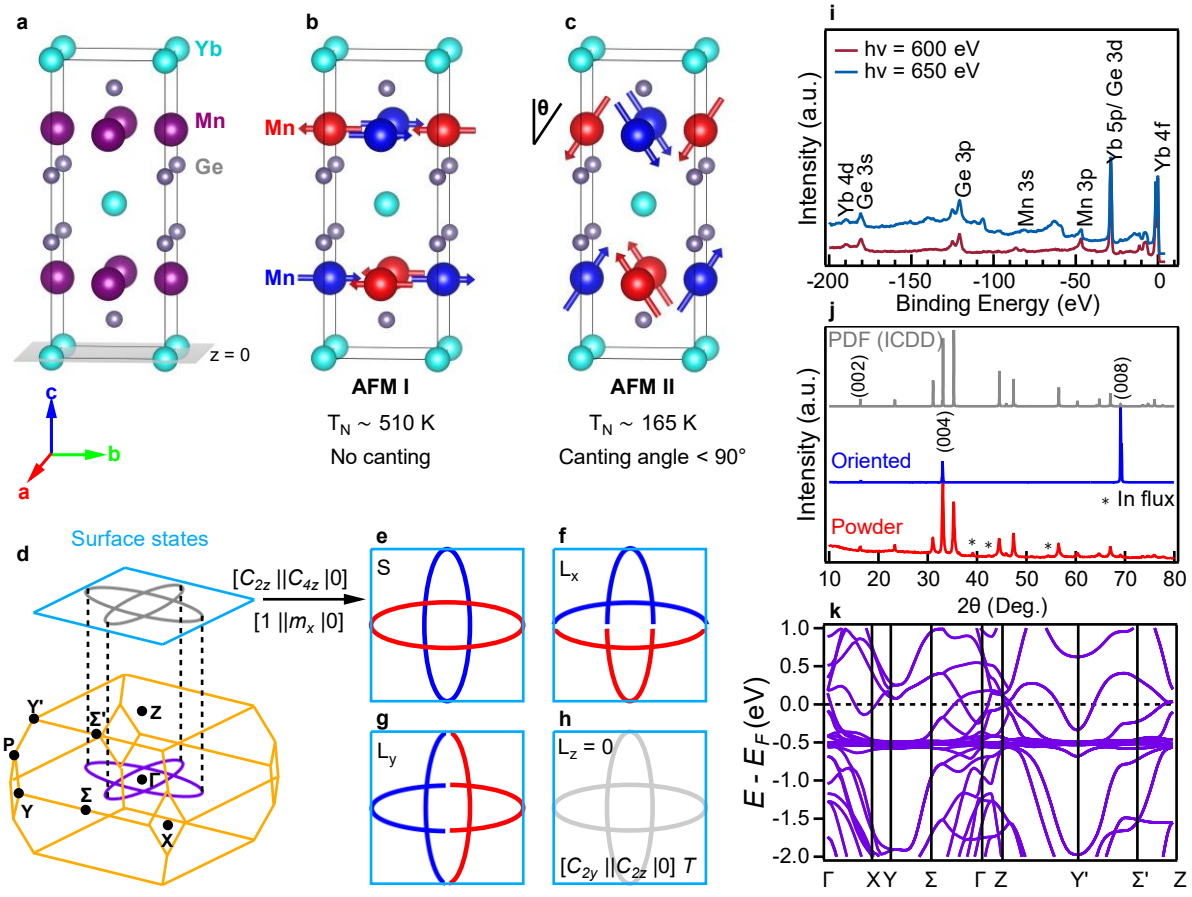


Fig. 1. Crystal structure, magnetic configurations, surface state symmetry, and basic characterizations of YMG. a. Tetragonal crystal structure of YMG highlighting Yb (cyan), Mn (purple), and Ge (grey) atomic positions. **b, c.** Magnetic structures in the high-temperature AFM I phase (b, T_{N1} ~ 510 K) with collinear Mn spins aligned along the in-plane axes without canting, and the low-temperature AFM II phase (c, T_{N1} ~ 165 K) exhibiting non-collinear spin canting with a canting angle $\theta < 90°$. **d.** 3D bulk Brillouin zone and corresponding projected (001) surface Fermi surface pockets. **e–h.** Theoretical symmetry classification and nodal structures of the projected surface states: **e.** spin textures S, **f, g.** in-plane orbital angular momentum textures L_x and L_y, and **h.** out-of-plane component $L_z = 0$. **i.** Core-level photoemission spectra measured at photon energies hv = 600 eV and 650 eV, resolving characteristic Yb 4f, Yb 5p, Ge 3d, Ge 3p, Ge 3s, Mn 3p, and Mn 3s sharp photoemission peaks. **j.** XRD patterns comparing ICDD PDF reference data (grey) with experimental single-crystal oriented diffraction showing sharp (00l) reflections (blue) and powder diffraction (red). Asterisks mark residual flux traces. **k.** Calculated DFT band structure along high-symmetry paths in the bulk Brillouin zone.

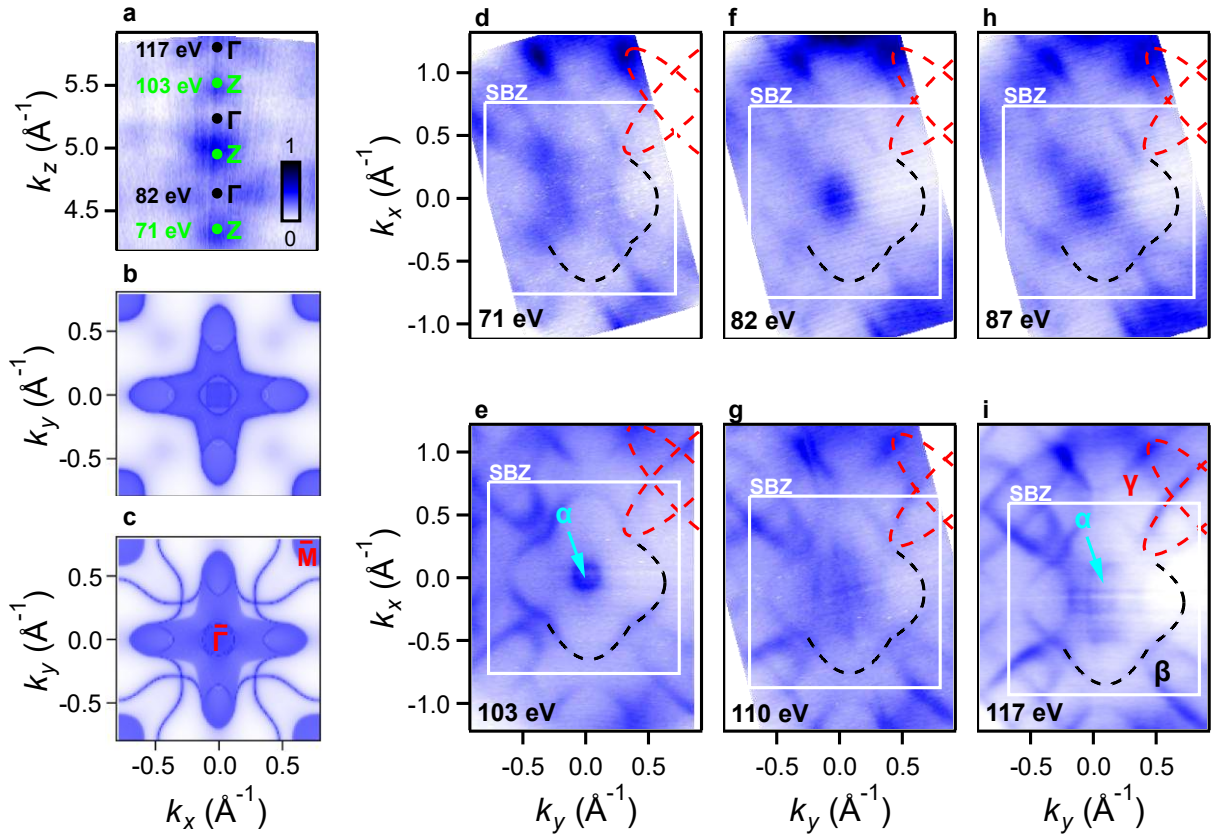


Fig. 2. Photon energy-dependent ARPES measurement and identification of surface states in YMG. a. Photon-energy-dependent ARPES intensity of Fermi surface map along the k_x-k_z plane. **b, c.** Calculated bulk and surface projection along (001) direction in the projected surface BZ, showing well-defined surface states. **d-i.** Fermi surface maps measured at various photon energies (71–117 eV). The white square denotes the surface BZ (SBZ) boundary.

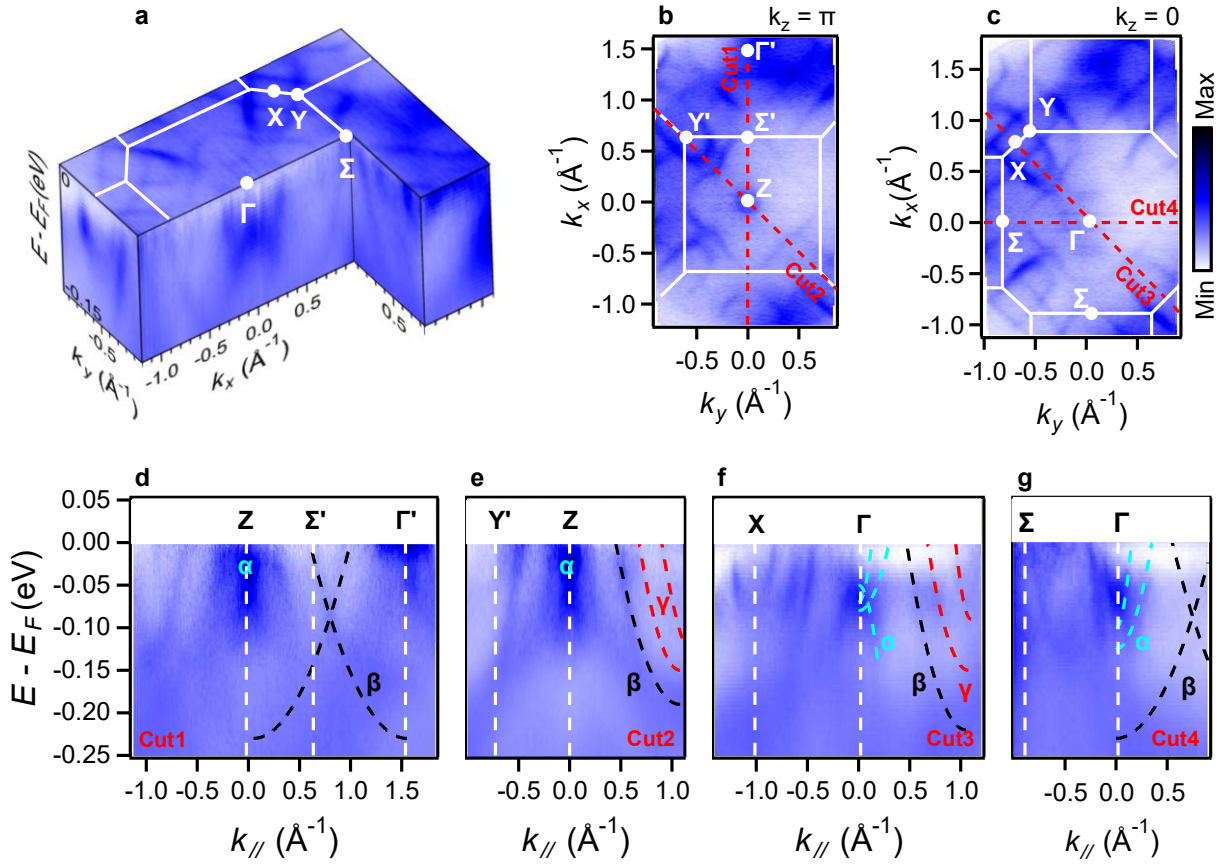


Fig. 3. 3D electronic band structure of YMG. a. 3D ARPES intensity plot of the low-energy electronic structure as a function of energy and momentum (E, k_x, k_y) in $k_z = 0$ plane. **b-c.** Fermi surface maps measured at $k_z = \pi$ and $k_z = 0$ planes, respectively. The white solid lines denote the boundaries of the BZ. **d-g.** Band dispersions along the high symmetry cuts indicated in **b** and **c**. Dashed lines trace the bulk α bands and the surface β and γ bands.

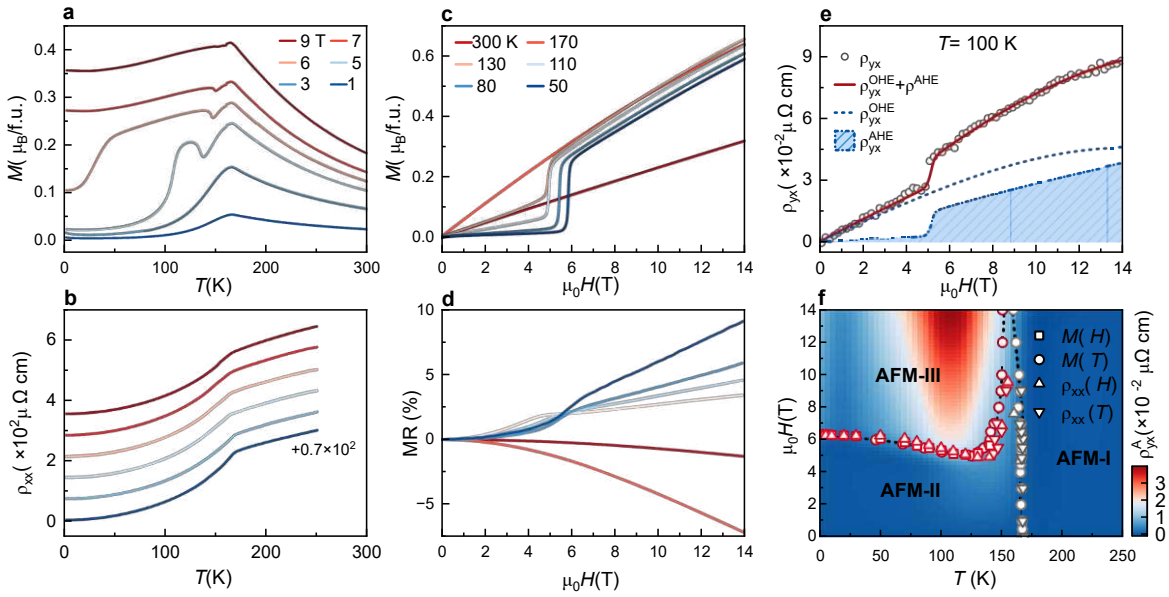


Fig.4. Transport and Thermodynamic Phase Diagram of Field-Induced Anomalous Hall Response. a Temperature dependence of magnetization M(*T*) under various out-of-plane magnetic fields (μ_0H = 1-9 T), showing distinct anomalies associated with magnetic phase transitions around $T_{N1} \approx 165$ K. **b** Temperature-dependent longitudinal resistivity ρ_{xx} under corresponding magnetic fields, stacked for clarity (+0.7 x 10^2 μΩ·cm offset per trace). **c.** Magnetic field dependent isothermal magnetization M measured up to 14T at temperatures ranging from 50 K to 300 K. At temperatures below 170 K, a sharp metamagnetic transition is observed at a critical field $\mu_0 H_c \approx$ 5-6 T. **d.** Normalized magnetoresistance $\rho_{xx}(T)$ showing a pronounced slope change and kink at the metamagnetic transition field. **e.** Representative Hall resistivity ρ_{yx} at T = 100 K fitted with a two-component model containing the ordinary Hall effect and the extracted anomalous Hall effect component (shaded region). **f.** Magnetic field–temperature (μ_0H /T) phase diagram overlaying the extracted anomalous Hall resistivity ρ_{yx}^{A} intensity map. Phase boundaries determined from M(H), M(T), ρ_{xx}(H), and ρ_{xx}(T) delineate three distinct antiferromagnetic regimes (**AFM-I**, **AFM-II**, **AFM-III**), showing that the emergent anomalous Hall state ($\rho_{yx}^{A} \neq 0$) is localized within the high-field **AFM-III** region bounded below $T_{N1} \approx 165$ K.

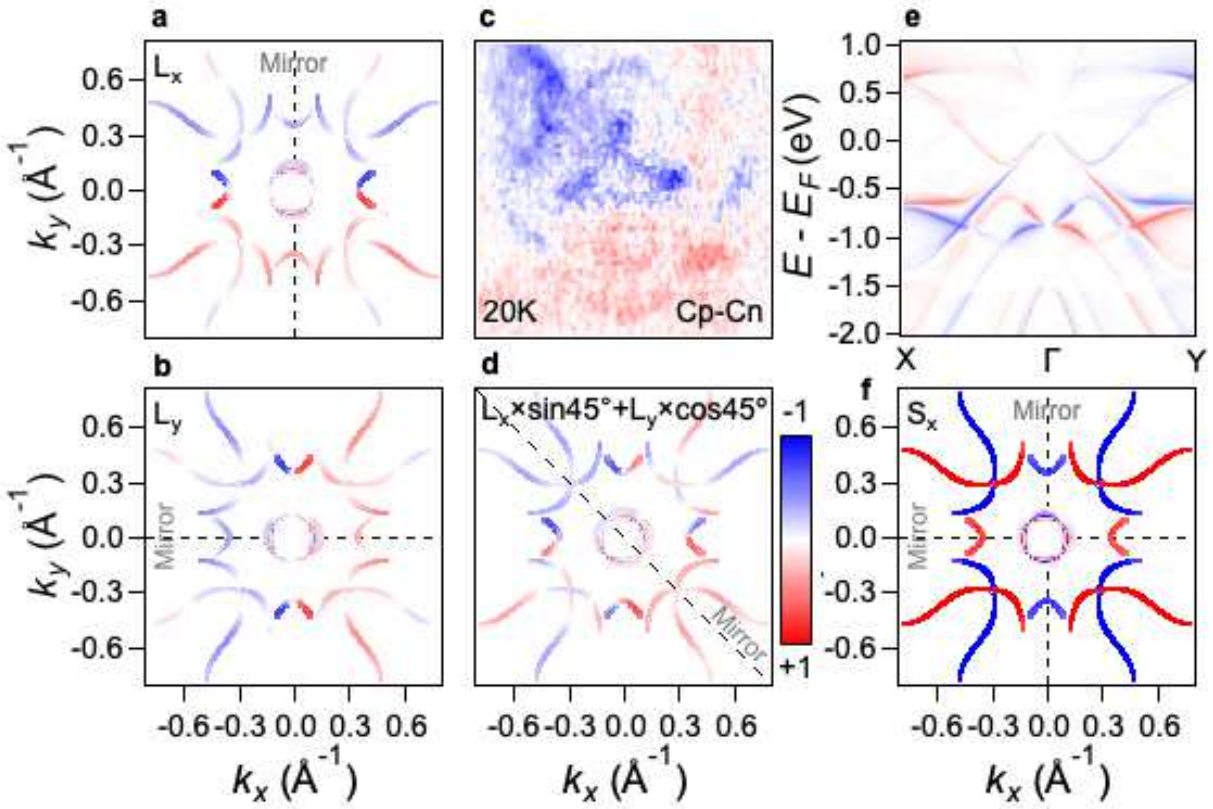


Fig. 5. Orbital and spin angular momentum textures of the surface states. a, b. Calculated momentum-space distribution of the in-plane orbital angular momentum (OAM) components **a** L_x and **b** L_y across the Fermi surface pockets in the k_x–k_y plane. **c.** Circular dichroism in CD-ARPES Fermi surface map measured at T = 20 K (Cp – Cn difference map), displaying a clear asymmetric intensity distribution across the Brillouin zone. **d.** Linear combination of the calculated in-plane OAM components (L_x sin 45° + L_y cos 45°) projected along the 110 direction, showing excellent qualitative agreement with the experimental CD-ARPES pattern in **d**. **e.** Theoretical band structure plotted along the high-symmetry path X–Γ–Y, showing bulk projection continuum alongside surface bands. **f.** Calculated momentum-dependent spin texture S_x across the Fermi surface contours, illustrating alternating spin polarization characteristic of the d-wave pattern.

References

1. Néel, L. Magnetism and local molecular field. *Science (1979).* **174**, 985–992 (1971).
2. Šmejkal, L., Sinova, J. & Jungwirth, T. Emerging research landscape of altermagnetism. *Phys. Rev. X* **12**, 040501 (2022).
3. Šmejkal, L., Sinova, J. & Jungwirth, T. Beyond conventional ferromagnetism and antiferromagnetism: A phase with nonrelativistic spin and crystal rotation symmetry. *Phys. Rev. X* **12**, 031042 (2022).
4. Wu, C. & Zhang, S.-C. Dynamic generation of spin-orbit coupling. *Phys. Rev. Lett.* **93**, 036403 (2004).
5. Wu, C., Sun, K., Fradkin, E. & Zhang, S.-C. Fermi liquid instabilities in the spin channel. *Phys. Rev. B* **75**, 115103 (2007).
6. Noda, Y., Ohno, K. & Nakamura, S. Momentum-dependent band spin splitting in semiconducting MnO_2: a density functional calculation. *Physical Chemistry Chemical Physics* **18**, 13294–13303 (2016).
7. Kriegner, D. *et al.* Multiple-stable anisotropic magnetoresistance memory in antiferromagnetic MnTe. *Nat. Commun.* **7**, 11623 (2016).
8. Naka, M. *et al.* Spin current generation in organic antiferromagnets. *Nat. Commun.* **10**, 4305 (2019).
9. Šmejkal, L., González-Hernández, R., Jungwirth, T. & Sinova, J. Crystal time-reversal symmetry breaking and spontaneous Hall effect in collinear antiferromagnets. *Sci. Adv.* **6**, eaaz8809 (2020).
10. Yuan, L.-D., Wang, Z., Luo, J.-W., Rashba, E. I. & Zunger, A. Giant momentum-dependent spin splitting in centrosymmetric low-*Z* antiferromagnets. *Phys. Rev. B* **102**, 014422 (2020).
11. Hayami, S., Yanagi, Y. & Kusunose, H. Bottom-up design of spin-split and reshaped electronic band structures in antiferromagnets without spin-orbit coupling: Procedure on the basis of augmented multipoles. *Phys. Rev. B* **102**, 144441 (2020).
12. Reichlová, H. *et al.* Macroscopic time reversal symmetry breaking by staggered spin-momentum interaction. Preprint at https://arxiv.org/abs/2012.15651 (2020).
13. Mazin, I. I., Koepernik, K., Johannes, M. D., González-Hernández, R. & Šmejkal, L. Prediction of unconventional magnetism in doped $FeSb_2$. *Proceedings of the National Academy of Sciences* **118**, e2108924118 (2021).

14. González-Hernández, R. *et al.* Efficient electrical spin splitter based on nonrelativistic collinear antiferromagnetism. *Phys. Rev. Lett.* **126**, 127701 (2021).

15. Naka, M., Motome, Y. & Seo, H. Perovskite as a spin current generator. *Phys. Rev. B* **103**, 125114 (2021).

16. Shao, D.-F., Zhang, S.-H., Li, M., Eom, C.-B. & Tsymbal, E. Y. Spin-neutral currents for spintronics. *Nat. Commun.* **12**, 7061 (2021).

17. Reimers, S. *et al.* Direct observation of altermagnetic band splitting in CrSb thin films. *Nat. Commun.* **15**, 2116 (2024).

18. Osumi, T. *et al.* Observation of a giant band splitting in altermagnetic MnTe. *Phys. Rev. B* **109**, 115102 (2024).

19. Zhu, Y.-P. *et al.* Observation of plaid-like spin splitting in a noncoplanar antiferromagnet. *Nature* **626**, 523–528 (2024).

20. Krempaský, J. *et al.* Altermagnetic lifting of Kramers spin degeneracy. *Nature* **626**, 517–522 (2024).

21. Lee, S. *et al.* Broken Kramers Degeneracy in Altermagnetic MnTe. *Phys. Rev. Lett.* **132**, 036702 (2024).

22. Han, L. *et al.* Electrical 180° switching of Néel vector in spin-splitting antiferromagnet. *Sci. Adv.* **10**, eadn0479 (2024).

23. Jungwirth, T., Marti, X., Wadley, P. & Wunderlich, J. Antiferromagnetic spintronics. *Nat. Nanotechnol.* **11**, 231–241 (2016).

24. Baltz, V. *et al.* Antiferromagnetic spintronics. *Rev. Mod. Phys.* **90**, 015005 (2018).

25. Liu, P., Li, J., Han, J., Wan, X. & Liu, Q. Spin-group symmetry in magnetic materials with negligible spin-orbit coupling. *Phys. Rev. X* **12**, 021016 (2022).

26. Rimmler, B. H., Pal, B. & Parkin, S. S. P. Non-collinear antiferromagnetic spintronics. *Nat. Rev. Mater.* **10**, 109–127 (2024).

27. Song, C. *et al.* Altermagnets as a new class of functional materials. *Nat. Rev. Mater.* **10**, 473–485 (2025).

28. Sødequist, J. & Olsen, T. Two-dimensional altermagnets from high throughput computational screening: Symmetry requirements, chiral magnons, and spin-orbit effects. *Appl. Phys. Lett.* **124**, 182409 (2024).

29. Zeng, S. & Zhao, Y.-J. Description of two-dimensional altermagnetism: Categorization using spin group theory. *Phys. Rev. B* **110**, 054406 (2024).

30. Ma, H.-Y. *et al.* Multifunctional antiferromagnetic materials with giant piezomagnetism and noncollinear spin current. *Nat. Commun.* **12**, 2846 (2021).

31. Jiang, B. *et al.* A metallic room-temperature d-wave altermagnet. *Nat. Phys.* **21**, 754–759 (2025).

32. Zhang, F. *et al.* Crystal-symmetry-paired spin–valley locking in a layered room-temperature metallic altermagnet candidate. *Nat. Phys.* **21**, 760–767 (2025).

33. Sun, Y. *et al.* Antiferromagnetic structure of KV_2Se_2O: A neutron diffraction study. *Phys. Rev. B* **112**, 184416 (2025).

34. Yang, G. *et al.* Observation of hidden altermagnetism in $Cs_{1-\delta}V_2Te_2O$. Preprint at https://arxiv.org/abs/2512.00972 (2026).

35. Mu, D. *et al.* Direct observation of quadruple spin-texture locking in a 2D d-wave altermagnet. Preprint at https://arxiv.org/abs/2604.18337 (2026).

36. Cheng, X., Gao, Y. & Liu, J. P. J. Realistic tight-binding model for V_2Se_2O-family altermagnets. Preprint at https://arxiv.org/abs/2602.09465 (2026).

37. Regmi, R. B. *et al.* Altermagnetism in the layered intercalated transition metal dichalcogenide $CoNb_4Se_8$. *Nat. Commun.* **16**, 4399 (2025).

38. Dale, N. *et al.* Relativistic and nonrelativistic spin splitting above and below the Fermi level in a g-wave altermagnet. Preprint at https://arxiv.org/abs/2411.18761 (2024).

39. Sakhya, A. P. *et al.* Electronic structure of a layered altermagnetic compound $CoNb_4Se_8$. Preprint at https://arxiv.org/abs/2503.16670 (2025).

40. He, R. *et al.* Nonrelativistic spin-momentum coupling in antiferromagnetic twisted bilayers. *Phys. Rev. Lett.* **130**, 046401 (2023).

41. Sheoran, S. & Dev, P. Spontaneous anomalous Hall effect in two-dimensional altermagnets. *Phys. Rev. B* **111**, 184407 (2025).

42. Wang, J. *et al.* Pentagonal 2D altermagnets: material screening and altermagnetic tunneling junction device application. *Adv. Funct. Mater.* **36**, 2505145 (2026).

43. Rahman, S., Torres, J. F., Khan, A. R. & Lu, Y. Recent Developments in van der Waals Antiferromagnetic 2D Materials: Synthesis, Characterization, and Device Implementation. *ACS Nano* **15**, 17175–17213 (2021).

44. Jana, N., Chakraborty, A., Mukherjee, A. & Agarwal, A. Layered topological antiferromagnetic metal at room temperature: $YbMn_2Ge_2$. *Phys. Rev. B* **112**, 075127 (2025).

45. Şaşıoğlu, E., Mertig, I. & Lounis, S. *d*-wave surface altermagnetism in centrosymmetric collinear antiferromagnets. *Phys. Rev. B* **114**, L020406 (2026).

46. Lange, C. *et al.* Emergent altermagnetism at surfaces of antiferromagnets: full symmetry classification and material identification. Preprint at https://arxiv.org/abs/2602.08773 (2026).

47. Qin, F. & Chen, R. Layer Hall effect induced by altermagnetism. *Phys. Rev. B* **113**, 165418 (2026).

48. Zhao, Y., Mandal, S., Liu, C.-X. & Yan, B. Emergent anomalous Hall effect from surface states in altermagnetic MnTe thin films. *Phys. Rev. B* **114**, 065304 (2026).

49. Zhou, L.-J. *et al.* Surface-State-Driven Anomalous Hall Effect in Altermagnetic MnTe Films. Preprint at https://arxiv.org/abs/2602.09363 (2026).

50. Fang, S. *et al.* One-dimensional electronics with edge states in two-dimensional altermagnets. *Phys. Rev. B* **113**, 224407 (2026).

51. Cheong, S.-W. & Huang, F.-T. Altermagnetism with non-collinear spins. *NPJ Quantum Mater.* **9**, 13 (2024).

52. Lin, Z. *et al.* Bulk band structure of RuO_2 measured with soft x-ray angle-resolved photoemission spectroscopy. *Phys. Rev. B* **111**, 134450 (2025).

53. Hao, Z. *et al.* Surface *d*-orbital order in an intermetallic compound. *Nat. Phys.* https://doi.org/10.1038/s41567-026-03359-4 (2026) doi:10.1038/s41567-026-03359-4.

54. Hofmann, M., Campbell, S. J. & Szytula, A. Antiferromagnetism in $YbMn_2Ge_2$–Mn magnetic sublattice. *J. Alloys Compd.* **311**, 137–142 (2000).

55. Fujiwara, T., Fujii, H., Koyama, K. & Motokawa, M. Novel magnetism on single crystalline $YbMn_2Ge_2$. *Physica B Condens. Matter* **312–313**, 864–866 (2002).

56. Hofmann, M., Campbell, S. J., Link, P., Fiddy, S. & Goncharenko, I. Valence and magnetic transitions in YbMn2Ge2—Pressure and temperature. *Physica B Condens. Matter* **385–386**, 330–332 (2006).

57. Nakama, T. *et al.* Effect of pressure on thermopower and electrical resistivity of $YbMn_2Ge_2$. *J. Phys. Conf. Ser.* **150**, 042135 (2009).

58. Qiao, Y. *et al.* Negative thermal expansion in $YbMn_2Ge_2$ induced by the dual effect of magnetism and valence transition. *NPJ Quantum Mater.* **6**, 49 (2021).

59. Su, W. P., Schrieffer, J. R. & Heeger, A. J. Solitons in Polyacetylene. *Phys. Rev. Lett.* **42**, 1698–1701 (1979).

60. Su, W. P., Schrieffer, J. R. & Heeger, A. J. Soliton excitations in polyacetylene. *Phys. Rev. B* **22**, 2099–2111 (1980).

61. Heeger, A. J., Kivelson, S., Schrieffer, J. R. & Su, W.-P. Solitons in conducting polymers. *Rev. Mod. Phys.* **60**, 781–850 (1988).

62. Xu, Y. et al. Filling-enforced obstructed atomic insulators. *Phys. Rev. B* **109**, 165139 (2024).

63. Xu, Y. et al. Three-dimensional real space invariants, obstructed atomic insulators and a new principle for active catalytic sites. Preprint at https://arxiv.org/abs/2111.02433 (2021).

64. Liu, E. et al. Giant anomalous Hall effect in a ferromagnetic kagome-lattice semimetal. *Nat. Phys.* **14**, 1125–1131 (2018).

65. Zeng, C., Yao, Y., Niu, Q. & Weitering, H. H. Linear Magnetization Dependence of the Intrinsic Anomalous Hall Effect. *Phys. Rev. Lett.* **96**, 037204 (2006).

66. Šmejkal, L., MacDonald, A. H., Sinova, J., Nakatsuji, S. & Jungwirth, T. Anomalous Hall antiferromagnets. *Nat. Rev. Mater.* **7**, 482–496 (2022).

67. Shockley, W. On the Surface States Associated with a Periodic Potential. *Physical Review* **56**, 317–323 (1939).

68. Fu, L. & Kane, C. L. Superconducting Proximity Effect and Majorana Fermions at the Surface of a Topological Insulator. *Phys. Rev. Lett.* **100**, 096407 (2008).

69. Kresse, G. & Furthmüller, J. Efficiency of ab-initio total energy calculations for metals and semiconductors using a plane-wave basis set. *Comput. Mater. Sci.* **6**, 15–50 (1996).

70. Perdew, J. P., Burke, K. & Ernzerhof, M. Generalized Gradient Approximation Made Simple. *Phys. Rev. Lett.* **77**, 3865–3868 (1996).

71. Kresse, G. & Joubert, D. From ultrasoft pseudopotentials to the projector augmented-wave method. *Phys. Rev. B* **59**, 1758–1775 (1999).

72. Mostofi, A. A. et al. An updated version of wannier90: A tool for obtaining maximally-localised Wannier functions. *Comput. Phys. Commun.* **185**, 2309–2310 (2014).

73. Wu, Q., Zhang, S., Song, H.-F., Troyer, M. & Soluyanov, A. A. WannierTools: An open-source software package for novel topological materials. *Comput. Phys. Commun.* **224**, 405–416 (2018).

Supplementary Files

This is a list of supplementary files associated with this preprint. Click to download.

- YMGSupplementaryMaterialsv6.2.docx